PFISR observation of intense ion upflow fluxes associated with an SED during the 1 June 2013 geomagnetic storm

Shasha Zou[1] (iD), **Aaron Ridley[1]**, **Xianzhe Jia[1]** (iD), **Emma Boyd[2]**, **Michael Nicolls[3]**, **Anthea Coster[4]** (iD), **Evan Thomas[5]** (iD), **and J. M. Ruohoniemi[6]** (iD)

[1]Department of Climate and Space Sciences and Engineering, University of Michigan, Ann Arbor, Michigan, USA, [2]Department of Aerospace Engineering, University of Michigan, Ann Arbor, Michigan, USA, [3]Center for Geospace Studies, SRI International, Menlo Park, California, USA, [4]Haystack Observatory, Massachusetts Institute of Technology, Westford, Massachusetts, USA, [5]Thayer School of Engineering, Dartmouth College, Hanover, New Hampshire, USA, [6]Department of Electrical and Computer Engineering, Virginia Polytechnic Institute and State University, Blacksburg, Virginia, USA

Abstract The Earth's ionosphere plays an important role in supplying plasma into the magnetosphere through ion upflow/outflow, particularly during periods of strong solar wind driving. An intense ion upflow flux event during the 1 June 2013 storm has been studied using observations from multiple instruments. When the open-closed field line boundary (OCB) moved into the Poker Flat incoherent scatter radar (PFISR) field of view, divergent ion fluxes were observed by PFISR with intense upflow fluxes reaching $\sim 1.9 \times 10^{14} \, m^{-2} \, s^{-1}$ at ~600 km altitude. Both ion and electron temperatures increased significantly within the ion upflow, and thus, this event has been classified as a type 2 upflow. We discuss factors contributing to the high electron density and intense ion upflow fluxes, including plasma temperature effect and preconditioning by storm-enhanced density (SED). Our analysis shows that the significantly enhanced electron temperature due to soft electron precipitation in the cusp can reduce the dissociative recombination rate of molecular ions above ~400 km and contributed to the density increase. In addition, this intense ion upflow flux event is preconditioned by the lifted *F* region ionosphere due to northwestward convection flows in the SED plume. During this event, the OCB and cusp were detected by DMSP between 15 and 16 magnetic local times, unusually duskward. Results from a global magnetohydrodynamics simulation using the Space Weather Modeling Framework have been used to provide a global context for this event. This case study provides a more comprehensive mechanism for the generation of intense ion upflow fluxes observed in association with SEDs.

1. Introduction

The terrestrial ionosphere plays an important role in supplying plasma into the magnetosphere through ion outflows, including heavy ions such as O^+ [e.g., *Yau and André*, 1997; *Moore and Horwitz*, 2007; *Lotko*, 2007]. The O^+ ions have been shown to be important in regulating the dynamics in the magnetosphere [*Kronberg et al.*, 2014, and references therein], such as altering the ion concentration in the ring current [e.g., *Daglis et al.*, 1999, and references therein] and affecting the substorm occurrence rate [e.g., *Brambles et al.*, 2011; *Liao et al.*, 2014]. Numerical simulation results also show that the source location of O^+ can affect its influence on the magnetospheric dynamics [*Yu and Ridley*, 2013].

Ion outflow may occur as a two-step process. The first step is the ion upflow in the topside ionosphere, which pumps plasma to higher altitudes ($> \sim 2000$ km); and then additional energization processes at those altitudes are able to continue accelerating plasmas to reach the escape velocity [e.g., *Strangeway et al.*, 2005]. The conversion rate from the ion upflow to the ion outflow has been suggested to range from 0.1% to 5% based on three conjugate observations from the Sondrestrom incoherent scatter radar and the FAST satellite [*Sánchez and Strømme*, 2014]. Near the dayside cusp regions, *Skjæveland et al.* [2014] showed that the probability of upflow events turning into outflows can reach 40% for strong flux events ($> 10^{13} \, m^{-2} \, s^{-1}$), under the assumption that plasmas reaching an altitude of >800 km can be further accelerated to the escape velocity. *Nilsson et al.* [2008] suggested that the initial ion upflow plays a critical role in determining the strength of ion outflow because the additional acceleration processes at higher altitudes seem common enough. Therefore, understanding the physical processes that generate intense ion upflow under various interplanetary and geomagnetic conditions is of great importance.

Based on the plasma temperature associated with the ion upflow in the *F* region and the topside ionosphere, ion upflow events have been conventionally classified into two categories, type 1 and type 2 [*Wahlund et al.*, 1992]. The type 1 ion upflows are related to strong perpendicular electric fields, enhanced and anisotropic ion temperatures, and low electron densities below 300 km. The enhanced ion temperature results in pressure gradients that propel the ions to higher altitudes. The type 2 ion upflows are related to electron precipitation, electron temperature increase, and reduced or unaffected topside electron density. The largely increased electron temperature in the topside ionosphere leads to an increased ambipolar electric field, and consequently ions are pulled upward together with the expanding electrons. The type 2 ion upflows can sometimes be accompanied by enhanced ion temperature as well.

Type 1 ion upflows are associated with frictional heating driven by strong perpendicular electric fields. The effects of these electric fields on the ionosphere have been studied extensively [e.g., *Sellek et al.*, 1991; *Heelis et al.*, 1993]. For instance, *Sellek et al.* [1991] used an ionosphere and plasmasphere model to study the effect of frictional heating due to a 2 km/s westward drift. Their results showed that the O^+ temperature increases from ~1000 K to ~3200 K between 200 km and 500 km, decreases rapidly from ~3200 K to ~2000 K between 500 km and 750 km, and shows no change above 750 km. Ionospheric O^+ density is rapidly (~5 min) depleted below 1000 km due to divergent plasma flows and increased O^+ loss rate. Similarly, *Heelis et al.* [1993] studied the effect of frictional heating of a 2 km/s horizontal drift on O^+ temperature and upflow velocity with focus on their transient dynamic evolutions. Their simulation results showed a negative temperature gradient between 300 km and 1000 km about several minutes after reaching the peak velocity.

Millward et al. [1999] showed that soft electron precipitation (50–100 eV) mainly produces ionization in the *F* region and the topside ionosphere. The effect of the soft particle precipitation in generating the type 2 ion upflows has also been extensively studied [e.g., *Richards*, 1995; *Su et al.*, 1999]. Modeling work conducted by *Su et al.* [1999] showed that both electron and ion temperatures in the topside ionosphere can be significantly enhanced due to soft electron precipitations (~100 eV), with much larger increase in the electron temperature. The model reproduced an inverse relationship between upward O+ fluxes and the characteristic energy of the precipitating electrons for the same energy flux level. In addition, the ion temperature shows a positive gradient in the *F* region and the topside ionosphere, in contrast to the negative ion temperature gradient seen in this region in the type 1 ion upflow simulations.

Both modeling and observational investigations have been carried out to distinguish the contributions from both mechanisms in producing ion upflows. Using the 1-D field line interhemispheric plasma model, *Liu et al.* [1995] conducted two case studies of the contributions of frictional heating induced upflow and electron precipitation induced upflow to observed values. They found that a combination of both mechanisms is required to produce the observed values and the soft electron precipitation plays a major role. Using DE 2 observations, *Seo et al.* [1997] found that the correlation between the upflow speed/flux and the electron temperature is higher than the correlation between either of the two quantities and the ion temperature and, therefore, suggested that soft electron precipitation is probably the primary driver. A similar conclusion has been reached by *Ogawa et al.* [2003] based on ~170 simultaneous events of European Incoherent Scatter (EISCAT) and DMSP observations. Furthermore, *Moen et al.* [2004] reported a one-to-one relationship between poleward moving auroral forms and ion upflows in the cusp and suggested that low-energy particle precipitation is the dominant energy source. Recently, contributions of the secondary electrons, which can be produced during photoionization or particle impact ionization to the formation of the ambipolar electric field, have also been studied [*Moore and Khazanov*, 2010; *Glocer et al.*, 2012].

The topside ionosphere density is usually enhanced within the storm-enhanced density (SED) region [*Foster et al.*, 2005; *Zou et al.*, 2013, 2014], which has been suggested to be the third mechanism of generating large ion upflow fluxes [*Lotko*, 2007; *Yau et al.*, 2011]. The first two mechanisms described above are due to plasma temperature increase, while this one associated with SED is due to increased plasma source population. Using the Dynamic Fluid Kinetic model, *Zeng and Horwitz* [2007] and *Zeng and Horwitz* [2008] studied the O^+ outflow due to cusp soft electron precipitation and the passage of a SED plasma flux tube through the cusp, respectively. They found that both mechanisms can produce a comparable amount of outflow. Observationally, a couple of fortuitous measurements have been reported that showed large ion upflow fluxes on the night side, which can be related to polar cap patches and SED. Using the Sondrestrom incoherent scatter radar, *Semeter et al.* [2003] reported a strong ion upflow event due to a drifting polar cap plasma
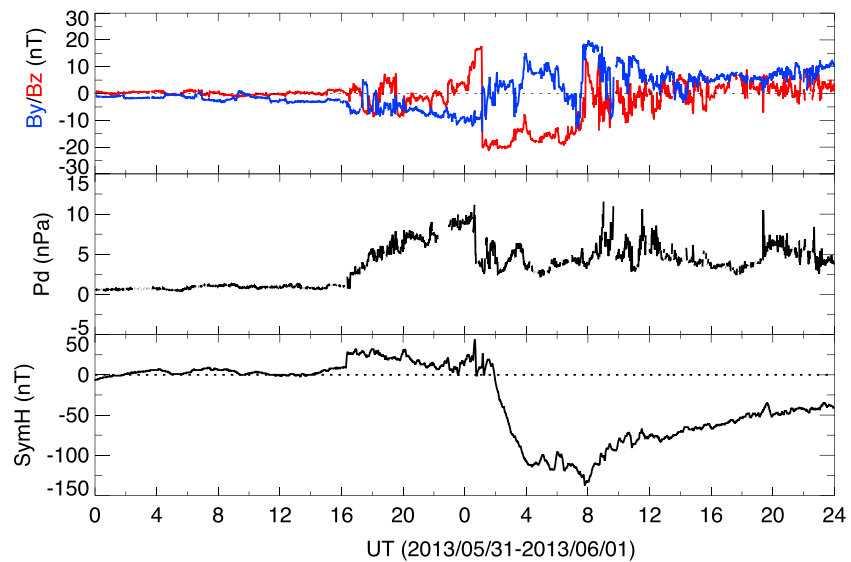
Figure 1. The IMF B_y (blue) and B_z (red) components in the GSM coordinates, the solar wind dynamic pressure P_d, and the *SYM-H* index for 31 May and 1 June 2013.

patch. The ion upflow speed exceeded 800 m/s at 900 km, and the associated ion upflow flux reached ~$1.4 \times 10^{14}\,m^{-2}\,s^{-1}$. Combining Global Positioning Satellite (GPS) total electron content (TEC) and DMSP satellite observations, *Yuan et al.* [2008] reported large field-aligned ion fluxes of ~$1.2 \times 10^{14}\,m^{-2}\,s^{-1}$ measured by a DMSP satellite within the SED when it reached the nightside polar cap boundary during the 20 November 2003 superstorm. When the SED plume disappeared in the polar cap, a significant reduction (~60%) of plasma density at high altitude between $3\,R_E$ and $6.5\,R_E$ has been reported by *Tu et al.* [2007] using the sounding measurements from the radio plasma imager on board IMAGE.

In the present study, we report on detailed observations of an ion upflow event that occurred during an intense geomagnetic storm on 1 June 2013. Observations from multiple instruments including Poker Flat incoherent scatter radar (PFISR) and DMSP are described in section 2. In addition, section 2 also shows results from a global magnetohydrodynamics (MHD) simulation using the Space Weather Modeling Framework (SWMF) [*Tóth et al.*, 2012], which provides a global context for this event in order to understand the magnetospheric field topology and the unusual location of the observed cusp-like precipitation. Discussions on the formation mechanisms of this intense ion upflow event are given in section 3, including plasma temperature effect and preconditioning by SED. Summary and conclusions are presented in section 4.

2. Observations and Modeling

2.1. Solar Wind and IMF Conditions

Figure 1 shows an overview of the interplanetary magnetic field (IMF) B_y and B_z components in the GSM coordinates, the solar wind dynamic pressure P_d, and the *SYM-H* index from 00 UT on 31 May to 24 UT on 1 June 2013. The solar wind and IMF data were obtained from the NASA/Goddard Space Flight Center's (GSFC) OMNI data set through the OMNIWeb and have been propagated to the nose of the bow shock. The solar wind dynamic pressure started to increase around 1600 UT on 31 May 2013 and initiated the storm sudden commencement signature in the *SYM-H* index. The main phase of the storm was triggered by the large IMF southward turning at ~0110 UT on 1 June 2013, and the IMF remained strongly southward afterward for ~7 h until ~0800 UT, when it turned back to northward. During the southward IMF interval, the IMF B_y component was positive most of the time. The *SYM-H* index reached the minimum of −137 nT at ~0800 UT, indicating an intense storm.

2.2. PFISR Observations

PFISR was running in the International Polar Year four-beam mode during this storm. Observations of beams 1, 2, and 4 in the long-pulse mode are shown in Figure 2 together with the beam location plots in magnetic
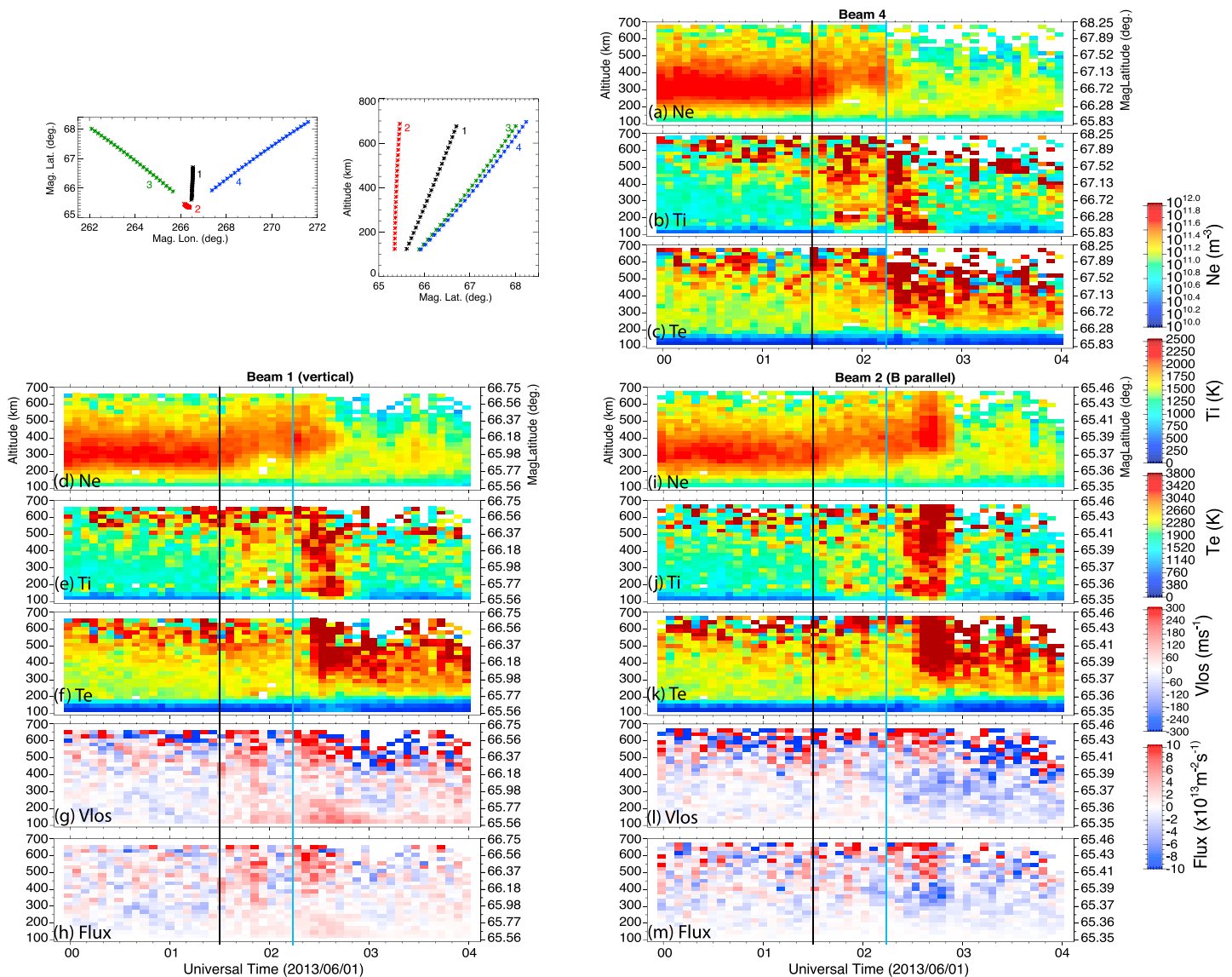
Figure 2. Observations from PFISR beams 1, 2, and 4 in the long-pulse mode are shown. Beams 3 and 4 are of lowest elevation angles looking at higher latitudes, beam 1 points in the vertical direction, and beam 2 is parallel to the magnetic field and located at the lowest latitude. (a–f and i–k) Altitude profiles of electron density (N_e), ion (T_i), and electron (T_e) temperatures. The (g and l) line-of-sight velocity (V_{los}) and the (h and m) ion flux, i.e., the product of N_e and V_{los}, are also shown for beam 2. The black vertical line indicates the starting time of the IMF southward turning, while the blue vertical line indicates the time of significant T_i and T_e increases seen in the topside ionosphere at beam 4 at ~0215 UT, respectively.

coordinates. Beams 3 and 4 are at lowest elevation angle and directed toward high latitudes. Beam 1 points in the vertical direction (90° elevation angle) in geographic coordinates, and beam 2 is parallel to the local magnetic field and located at the lowest latitude. Figures 2a–2c, 2d–2f, and 2i–2k show the altitude profiles of electron density (N_e), ion (T_i), and electron (T_e) temperatures for beams 4, 1, and 2, respectively. The line-of-sight velocity (V_{los}) and the ion flux, i.e., the product of N_e and V_{los}, are also shown for the lower latitude vertical beam (beam 1) and field-aligned beam (beam 2). In Figures 2g and 2l, positive values refer to line-of-sight flows pointing to higher altitudes along the beams. The ion flows/fluxes obtained from beam 2 measurements showed divergent flows/fluxes moving away from ~450 km altitude between ~0230 and 0250 UT. The ion upflow fluxes reached ~1.9×10^{14} m^{-2} s^{-1} at ~600 km, which is comparable to the largest ion upflow fluxes reported in *Semeter et al.* [2003] and *Yuan et al.* [2008].

Plasma temperature increases and their sharp equatorward boundaries have been suggested to be an indicator of the open-closed field line boundary (OCB) at the ionospheric altitudes [*Pryse et al.*, 2000]. During this

event, as the OCB expanded equatorward, the cusp signatures were seen first by beams at higher latitudes (e.g., beam 4) and subsequently by those at lower latitudes (e.g., beam 2). The black vertical line indicates the starting time of the IMF southward turning, while the blue vertical line indicates the time of significant T_i and T_e increases seen in the topside ionosphere at beam 4 at ~0215 UT. The time lag of the plasma temperature increase signature in beam 4 and beam 2 was about 10–15 min. Above ~300 km, both T_i and T_e observed by beam 2 showed increases in the topside ionosphere, and both had positive gradient in the vertical direction, indicating the existence of downward heat flux at the topside of the ionosphere. Below ~300 km, there were also episodic T_i increases, while T_e did not show much change. Plasma temperatures and their effects on electron densities are further discussed in section 3.

Figure 3 shows the PFISR measurements from 00 to 06 UT on 1 June 2013. From top to bottom, the $E \times B$ convection flow direction (a), magnitude (b), vector (c), the vertical flow (d) calculated combining the contributions from both the $E \times B$ convection flow and the antiparallel flow, the latitudinally averaged vertical flow (e) contributed by the convection flow ($V_{\text{up\_E}\times B}$, solid) and the antiparallel flow ($V_{\text{up\_ap}}$, dotted), and the electron density measured by beam 4 (f) and beam 1 (g) are shown. The method used to calculate the convection and antiparallel flows is described in *Heinselman and Nicolls* [2008]. The antiparallel flow is defined as positive when the flow is pointing to higher altitudes and along the magnetic field line in the Northern Hemisphere. Given a nonvertical magnetic field, both the $E \times B$ convection flow and the antiparallel flow can have a finite component in the geographic vertical direction. The total vertical flow is the sum of both contributions, as shown in Figure 10 of *Zou et al.* [2014].

Shortly after the IMF southward turning at 0110 UT measured at the bow shock nose, the convection pattern started to expand moving into the PFISR field of view (FOV), as evidenced by the increase of the convection flow speed at ~68° at ~0130 UT (magenta vertical line). The lifting effect of the ionosphere due to the enhanced northward component of the convection flow is evident in density observed by the vertical beam 1 shown in Figure 2d.

We calculate the ambipolar diffusion velocity using equation (1) [e.g., *Buonsanto and Witasse*, 1999; *Aponte et al.*, 2005] for altitudes where the O$^+$ abundance is >90%.

$$V_d = -2D_{\text{in}} \frac{T_p}{T_r} \sin I \left(\frac{1}{n_e} \frac{dn_e}{dz} + \frac{1}{T_p} \frac{dT_p}{dz} + \frac{0.36}{T_r} \frac{dT_r}{dz} + \frac{1}{H_p} \right), \tag{1}$$

where I is the magnetic dip angle, D_{in} is the ion-neutral diffusion coefficient given by $D_{\text{in}} = \frac{K_b T_r}{m_i \nu_{\text{in}}}$, $T_p = \frac{(T_i + T_e)}{2}$, $T_r = \frac{(T_i + T_n)}{2}$, and $H_p = \frac{2K_b T_p}{m_i g}$ is the plasma scale height. T_i, T_e, and N_e are observed by PFISR, while T_n and the abundances of O, O$_2$, and N$_2$ are obtained from the NRL-MSISE-00 model [*Picone et al.*, 2002]. The ion-neutral collisional frequency (ν_{in}) is the sum of collision frequencies between the atomic oxygen and three major atomic and molecular species. That is,

$$\nu_{\text{in}} = \nu_{\text{O}^+,\text{O}} + \nu_{\text{O}^+,\text{N}_2} + \nu_{\text{O}^+,\text{O}_2}. \tag{2}$$

Using equation (1), we have determined the contributions from four different terms, as shown in Figure 4. Plasma parameters measured by PFISR during the period of divergent ion flows between 0230 and 0245 UT are averaged and then smoothed by using a five-point running average in the parallel direction in order to reduce the noisiness of the data. As can be seen in Figure 4, the density gradient term, i.e., the first term in the parenthesis in the diffusion equation (1), contributes most strongly to the divergent flows at altitudes ≥475 km. However, the total calculated flows are not able to reproduce the observed field-aligned velocities. Possible reasons for this discrepancy may include uncertainties in the calculation of the ion-neutral collisional frequency, ISR measurement uncertainties, and the averaging and smoothing processes used to reduce the noisiness of the data.

2.3. DMSP Observations

Both the DMSP F16 and F17 satellites were in the late afternoon to early morning orbit during this storm. They observed precipitating particles (energy range between 32 eV and 30 keV) three times between ~02 and ~04 T and within an hour of magnetic local time (MLT) west of PFISR. Figure 5 shows the total precipitating electron (black) and ion (red) energy fluxes, their average energies, and energy spectra. During each pass, DMSP observed dispersive energetic ions and intense soft precipitating electron fluxes, which are classic signatures of precipitating particles originating from reconnection sites at the
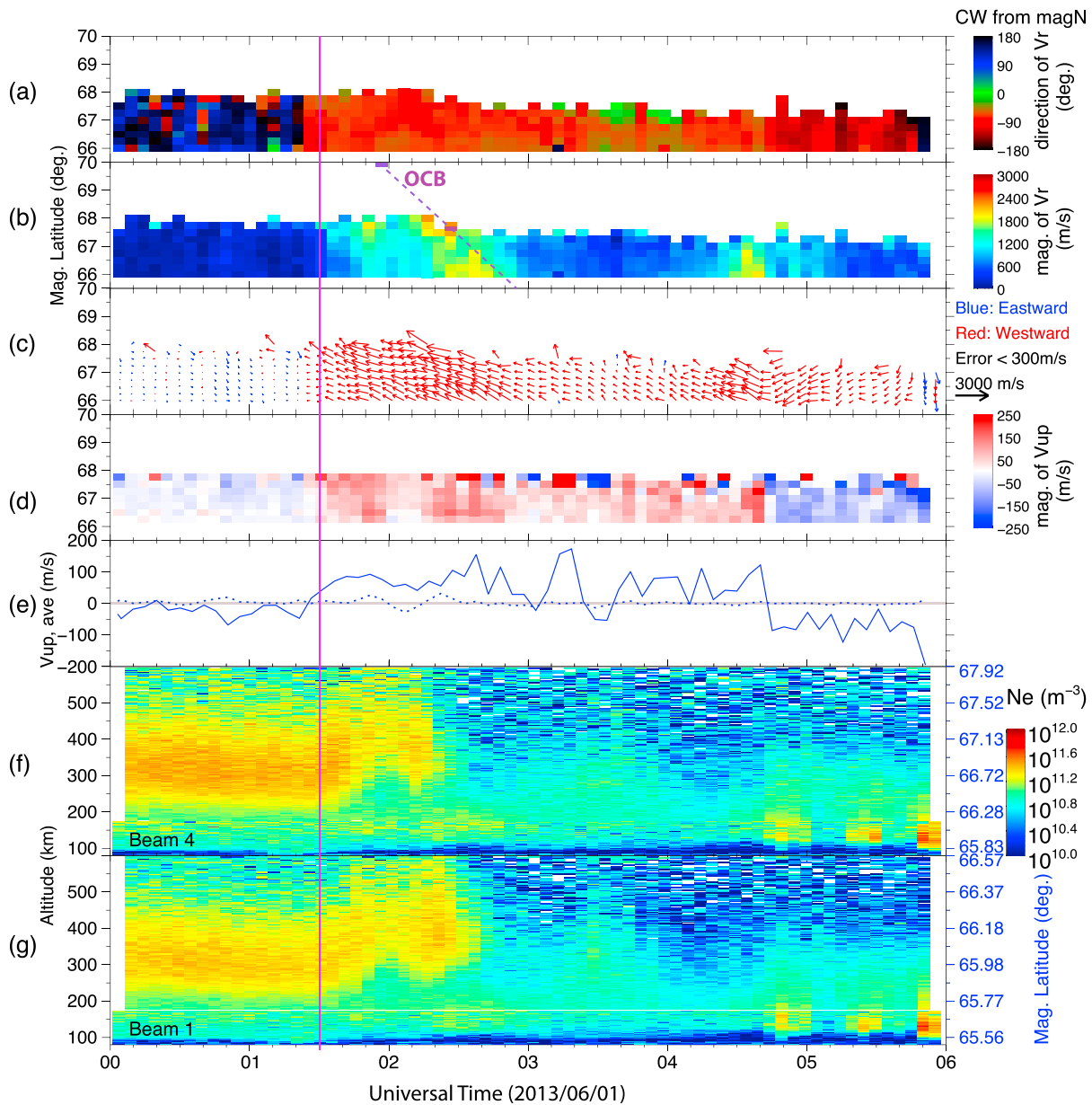
Figure 3. PFISR measurements from 00 to 06 UT on 1 June 2013. The $E \times B$ convection (a) flow direction, (b) magnitude, (c) vector, (d) the vertical flow, (e) the latitudinally averaged vertical flow contributed from the convection flow (solid) and the antiparallel flow (dotted), and the raw electron density with no correction for Te/Ti or Debye length effects measured by (f) beam 4 and (g) beam 1 are shown. Contributions from both convection flow and the antiparallel flow are combined to calculate the vertical flow. Electron density below 175 km is from the alternating code pulse measurement, while that above 175 km is from the long pulse measurement.

magnetopause. The ion dispersion signature, i.e., higher-energy particles reaching the DMSP satellite first and lower energy ones arriving later, is a well-known result of the velocity filter effect [e.g., *Reiff et al.*, 1977]. Once the magnetic field line becomes open, the magnetosheath electrons can move along the magnetic field line and precipitate into the ionosphere. Thus, the OCB can be determined by identifying the equatorward edge of the sheath-like precipitating electron population. During this event, the OCB was detected around 15 MLT three times, i.e., at 69.87° MLAT/1506 MLT at ~0158:38 UT, at 67.73° MLAT/1446 MLT at ~0222:22 UT, and at 62.70° MLAT/1544 MLT at ~0339:17 UT. These DMSP observations demonstrate that the OCB was initially poleward of the PFISR FOV and then expanded and crossed PFISR after the IMF turned strongly southward.
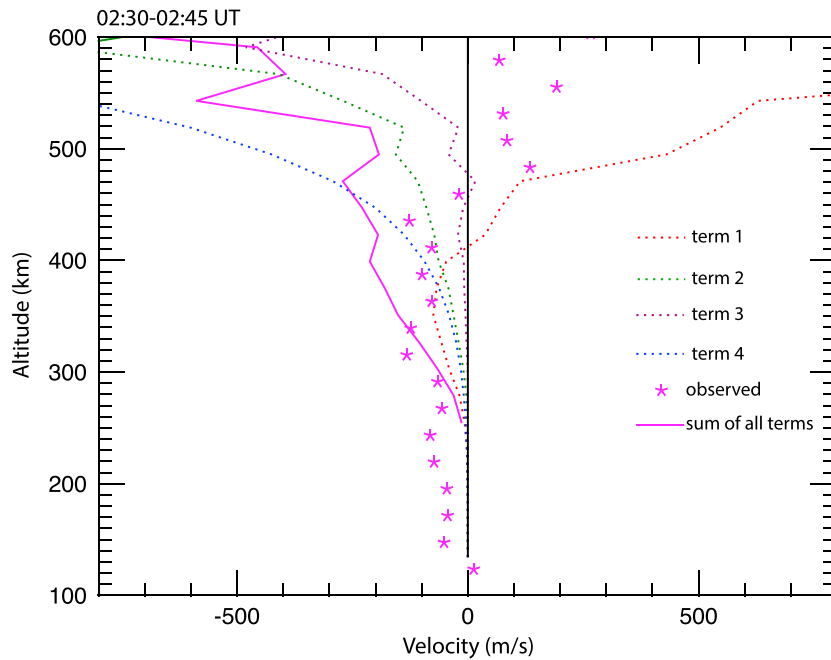
Figure 4. Observed and calculated field-aligned ion flows. Magenta asterisks represent the average of the observed values between 0230 and 0245 UT. Contributions from the four different terms in equation (1) are shown by different colors. Magenta line represents the sum of all terms.

2.4. MHD Modeling of OCB

This diverging field-aligned ion flow event is similar to those observed by the EISCAT Svalbard radar [*Buchert et al.*, 2004], and their statistical study showed that the occurrence rate for such diverging flow is extremely low at this MLT. In addition, the DMSP observations shown in Figure 5 were acquired around 16 MLT, which is unusual for cusp-like particle precipitation. In order to understand the mechanism responsible for the presence of cusp-like precipitation at this MLT, we have performed a global magnetosphere simulation with the solar wind input shown in Figure 1 using the Space Weather Modeling Framework (SWMF) developed at the University of Michigan [*Tóth et al.*, 2012].

The global MHD model within the SWMF, Block-Adaptive-Tree-Solar Wind-Roe-Upwind-Scheme (BATSRUS) [*Powell et al.*, 1999; *Gombosi et al.*, 2002, 2004], solves the governing MHD equations in a prescribed simulation domain, which typically extends about $30\,R_E$ upstream, a few hundred Earth radii downtail, and about $60\,R_E$ on the flank side. The inner boundary of the model is a sphere of radius $\sim2.5\,R_E$. BATSRUS uses an adaptive, block-based grid [*Tóth et al.*, 2012], allowing the user/the code itself to specify/determine the desired spatial resolution. BATSRUS has been two-way coupled with the Rice Convection Model [*De Zeeuw et al.*, 2004] and the Comprehensive Ring Current Model (CRCM) [*Buzulukova et al.*, 2010; *Glocer et al.*, 2013]. For the simulation performed for this event, we have used the coupled BATSRUS-CRCM model. In this model, the inner magnetosphere domain receives plasma boundary conditions and magnetic field geometry from BATSRUS and the electric field from the ionospheric electrodynamics (IE) solver [*Ridley et al.*, 2004] and then feeds hot plasma densities and pressures back to the BATSRUS MHD model. This IE module receives field-aligned currents from BATSRUS to calculate particle precipitation and conductance based on empirical relationships and then solves for the electric potential on a 2-D spherical grid [*Ridley and Liemohn*, 2002; *Ridley et al.*, 2004]. The electric field patterns are then passed back to all other physics domains within the SWMF.

Figures 6a–6c show the 3-D magnetic field topology of the magnetosphere and the plasma pressure distribution in the noon-midnight meridian for three selected times when the DMSP satellites passed Alaska on 1 June 2013, as viewed from ~21 MLT on the duskside. Figures 6d–6f show the modeled ionospheric convection pattern and the distribution of field-aligned currents at times corresponding to those of Figures 6a–6c. The ionospheric plots are shown in magnetic local time (MLT) and geomagnetic latitude (MLAT) coordinates with 12 MLT/18 MLT at the top left. The solid grey traces in Figures 6d–6f mark the open-closed field line
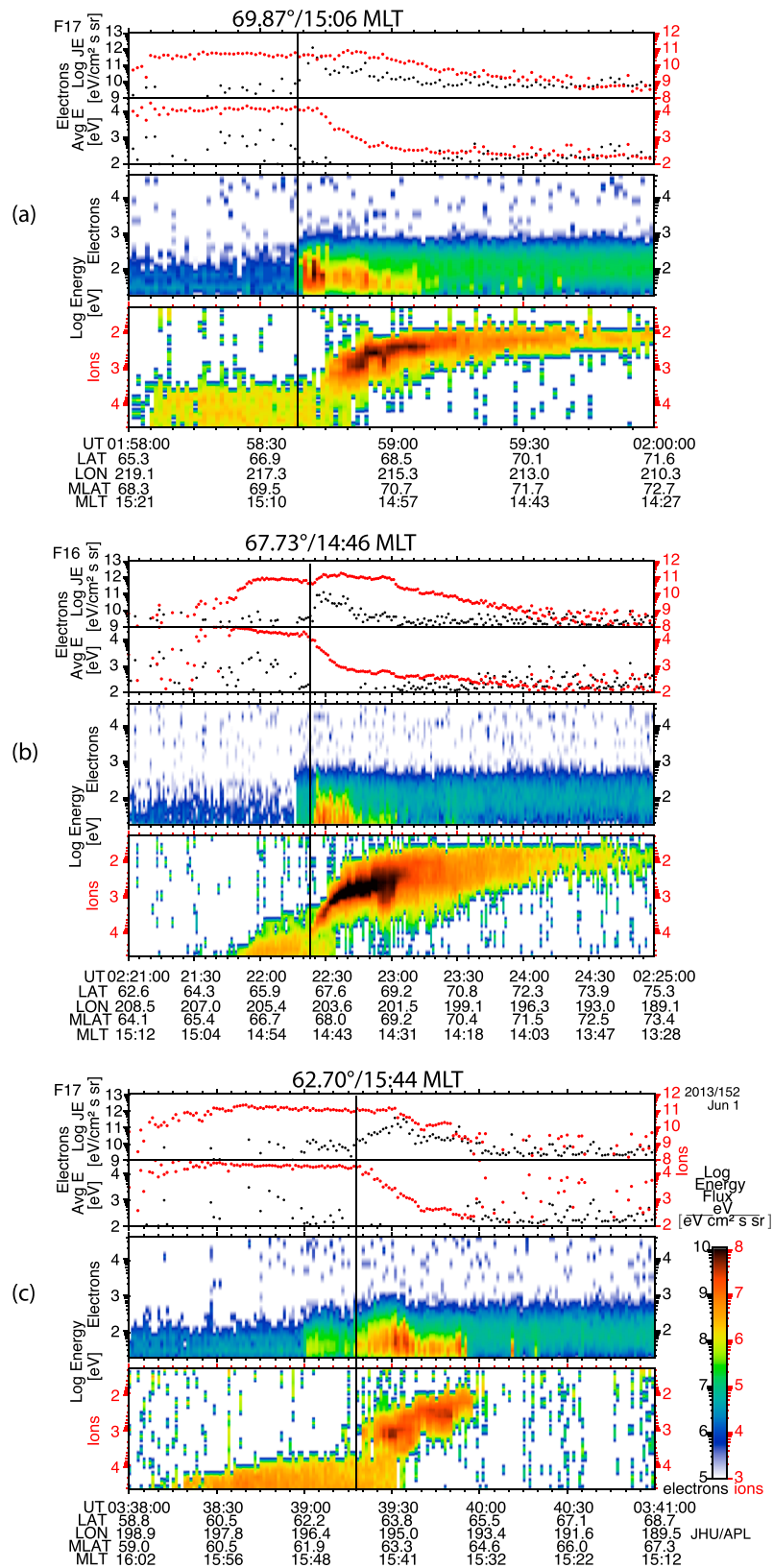
Figure 5. Total precipitating electron (black) and ion (red) energy fluxes, their average energies and differential energy fluxes from 32 eV to 30 keV measured by the DMSP Special Sensor Precipitating Electron and Ion Spectrometer particle detectors [*Hardy et al.*, 1984] during three passes near PFISR.
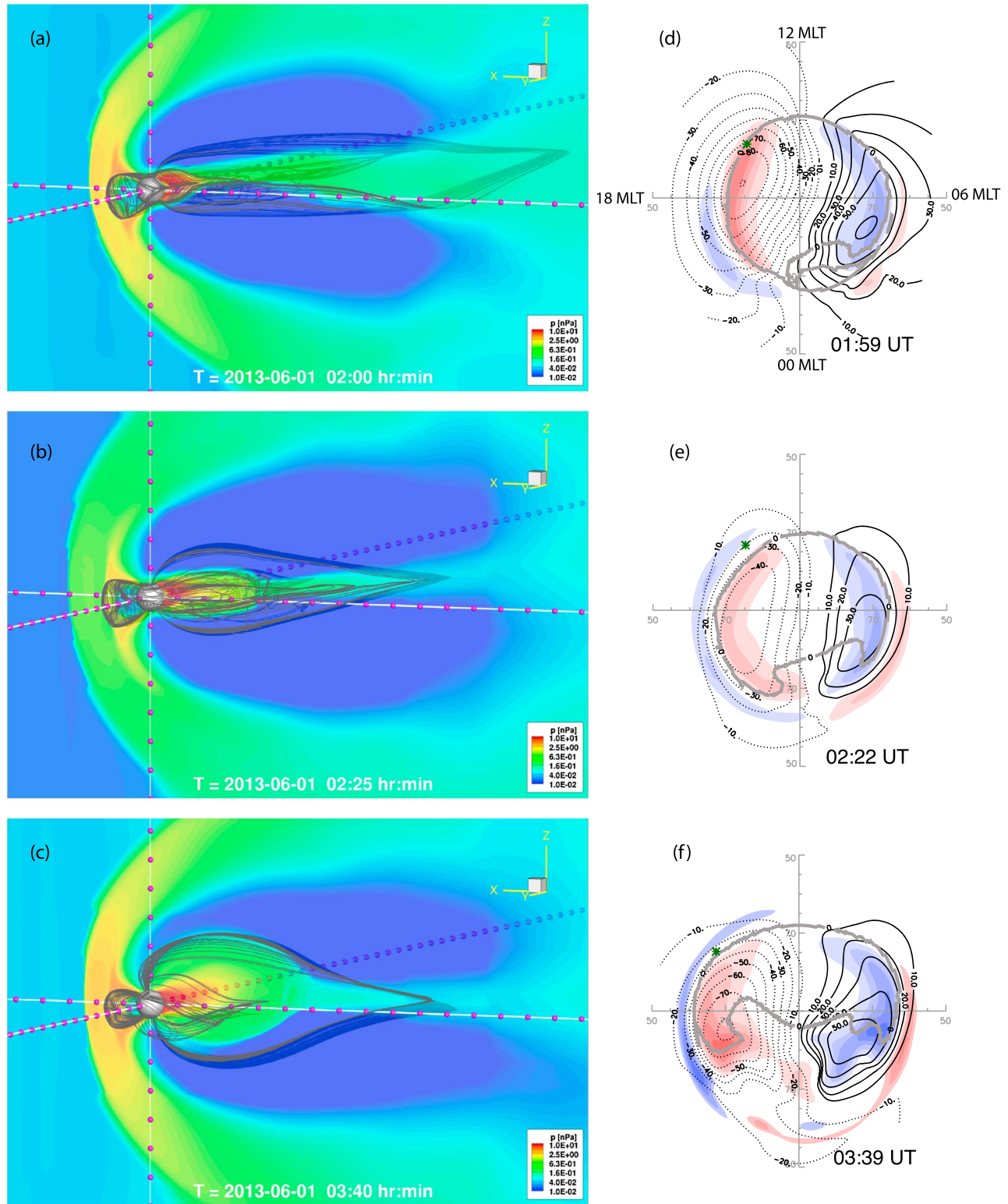
Figure 6. (a–c) Results from the coupled BATSRUS and CRCM simulation from three selected times when the DMSP satellites passed Alaska showing the last closed field lines traced at all local times as well as the color contours of plasma pressure in the noon-midnight meridian (viewed from ~21 local time on the dusk flank). The white sphere at the origin represents the inner boundary of the magnetosphere model, and the magenta balls mark off every 5 R_E on the axes. (d–f) Ionospheric properties extracted from three selected times when the DMSP satellites passed Alaska. Shown in each panel are color contours of the field-aligned current density overlaid with lines of equipotentials representing the ionospheric convection (thin solid and dotted lines). The thick grey trace in each panel shows the open-closed field line boundary (OCB) identified in the simulation, while the asterisks indicate the location where the DMSP satellites crossed the OCB.
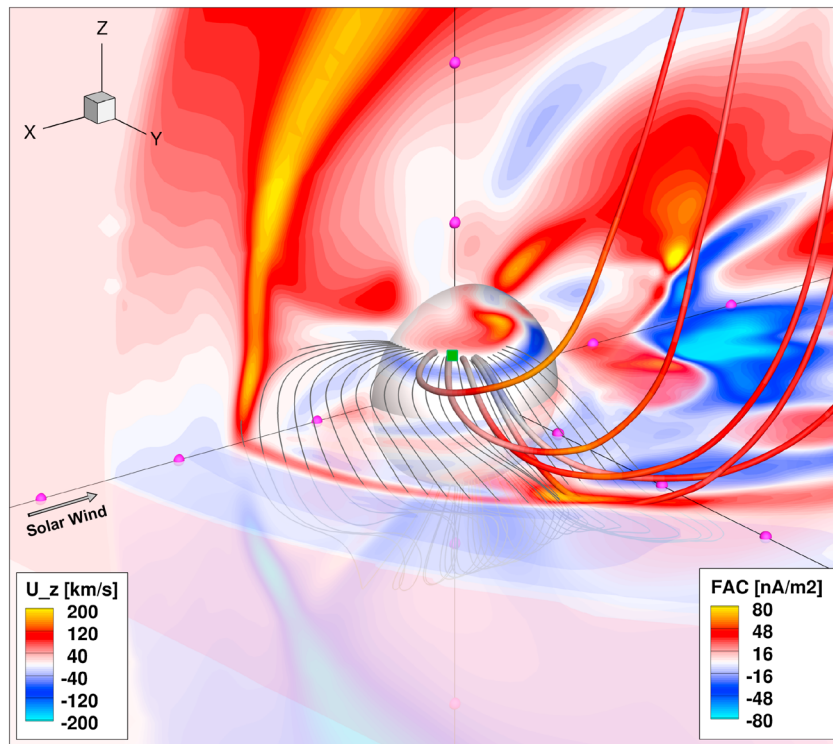
Figure 7. A 3-D view of the simulated magnetosphere extracted from the time step when the DMSP crossed the open-closed field line boundary. Shown in the two cut planes (*XZ* at *Y* = 0 and *XY* at *Z* = 0.5 R_E) are color contours of the *z* component of the plasma velocity (U_z). Colors on the sphere with a radius of 3 R_E are contours of the field-aligned current density (positive values mean upward field-aligned currents). The black thin lines represent the last closed field lines in the afternoon local time sector extracted from the simulation, while the thick tubes (which are color coded with U_z) show sample field lines near the footprint of the DMSP satellite (shown as the green square) around this time. The three GSM axes are labeled with magenta balls every 5 R_E.

boundary (OCB) traced at all local times. During this period, the IMF B_z was strongly southward (-20 nT) and the solar wind Mach number was very low (~4). Comparing the three snapshots of the open-closed field line boundary shows that the dayside magnetosphere was eroded gradually as the IMF turned strongly southward. The green asterisks in Figures 6d–6f mark the OCB determined based on the DMSP measurements. The global MHD model reproduced the location of the OCB very well at both the start and end time of the polar cap expansion, although the polar cap in the model opened up at a rate slower than that suggested by the observations.

To gain further insight into the large-scale structure of the magnetosphere around the time when DMSP detected cusp-like particle precipitation, we show in Figure 7 a 3-D view of the simulated magnetospheric configuration extracted from the time step corresponding to Figures 6c and 6f. Soft electron precipitation and dispersive ion precipitation in the cusp are suggested to map directly to reconnection sites at the dayside magnetopause [*Reiff et al.*, 1977], and these particle precipitation signatures are usually observed at low altitudes just poleward of the OCB. In Figure 7, the location of the DMSP satellite mapped along magnetic field line to the sphere of a radius of 3 R_E is marked by the green square. Field lines traced in the vicinity of the DMSP magnetic footprint show that they are open field lines with one end connected to the ionosphere and the other to the solar wind. As indicated by the colors showing the *z* component of the plasma velocity (V_z), those field lines move northward at speeds of about 200 km/s, which is of the order of the local Alfvén speeds. Both the flow direction and speed associated with the open flux tubes are consistent with them being generated by magnetopause reconnection under strongly southward IMF conditions. The high-speed flows associated with reconnection jets can also be seen around ~16–18 MLT in the near-equatorial plane in Figure 7. Equatorward of the DMSP footprint are closed field lines (black solid lines) that have both ends connected to the ionosphere. The magnetic field topology as shown by our global MHD model, therefore, confirms that during the interval when DMSP observed cusp-like particle signatures, the satellite was
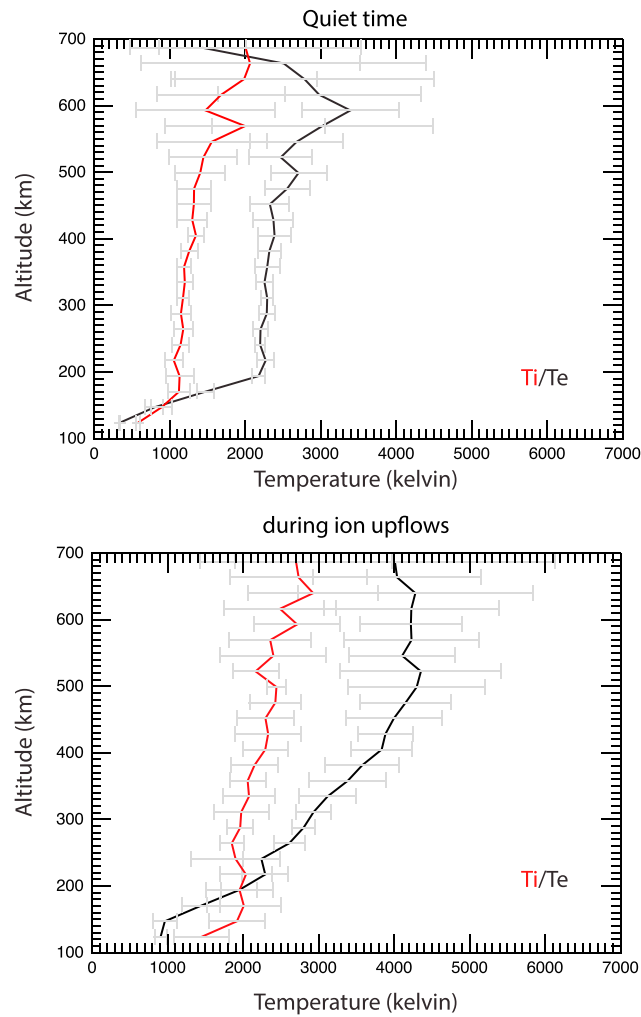
Figure 8. Average ion and electron temperatures during (a) quiet time and (b) ion upflows. PFISR measurements between 00 and 01 UT on 1 June 2013 are used to obtain quiet time plasma temperature profiles.

located very close to the open-closed field line boundary and that magneto-pause reconnection occurred in the late afternoon sector that produced open field lines that are magnetically connected to the DMSP satellite.

3. Discussion

3.1. Ion Upflow Event Classification

The pioneer work by *Wahlund et al.* [1992] suggested that plasma temperature profiles can be used for the classification of upflow events. In the 1 June ion upflow event presented here, both ion and electron temperature increases have been observed by PFISR. The ion and electron temperatures during both quiet time and heating time were averaged to quantify their variations. PFISR measurements between 00 and 01 UT on 1 June 2013 are used to obtain quiet time plasma temperature profiles and are shown in Figure 8a, while those during upflow time (0230–0250 UT) are shown in Figure 8b. As one can see, T_i and T_e during quiet time were ~1000 K and ~2000 K, respectively, and increased to >2000 K and >4000 K, respectively, during the upflow event.

Previous simulation studies suggested that the gradient of ion temperature in the topside ionosphere (>500 km) is negative for frictional heating event [e.g., *Sellek et al.*, 1991; *Heelis et al.*, 1993] and positive for soft electron precipitation [e.g., *Su et al.*, 1999]. Therefore, the altitude profile of the ion temperature within ion upflow can be used to distinguish between different heating mechanisms. In addition, the electron temperature vertical profile in this case is consistent with a heat source coming from the top [*Schunk and Nagy*, 2009]. Therefore, the positive gradients in the topside ionosphere in the T_i vertical profiles observed between 0230 and 0250 UT shown in Figure 8b are due to soft electron precipitation in the cusp and the subsequent heat transfer from electrons to ions. The DMSP observations in Figure 5 show intense particle fluxes with energies <100 eV. Particles with energies <100 eV contribute mainly to the heating of the ambient electrons and not much to the ionization. Therefore, DMSP observations are consistent with the temperature vertical profiles measured by PFISR.

After the convection flows increase starting at 0130 UT, the episodic T_i increases below 300 km without simultaneous T_e increase were caused by frictional heating. Frictional heating likely contributes to the T_i increase in the topside ionosphere but should not be the major heating mechanism based on its altitude profile. Based on the discussions above, this ion upflow event is likely mainly due to soft electron precipitation and thus should be categorized as a type 2 ion upflow event.

3.2. Enhancement of Topside Ionospheric Density Within Ion Upflows

During the 1 June ion upflow event, which we classify as a type 2 upflow event based on the discussion in the previous section, the topside ionospheric density increased, rather than decreased or remained
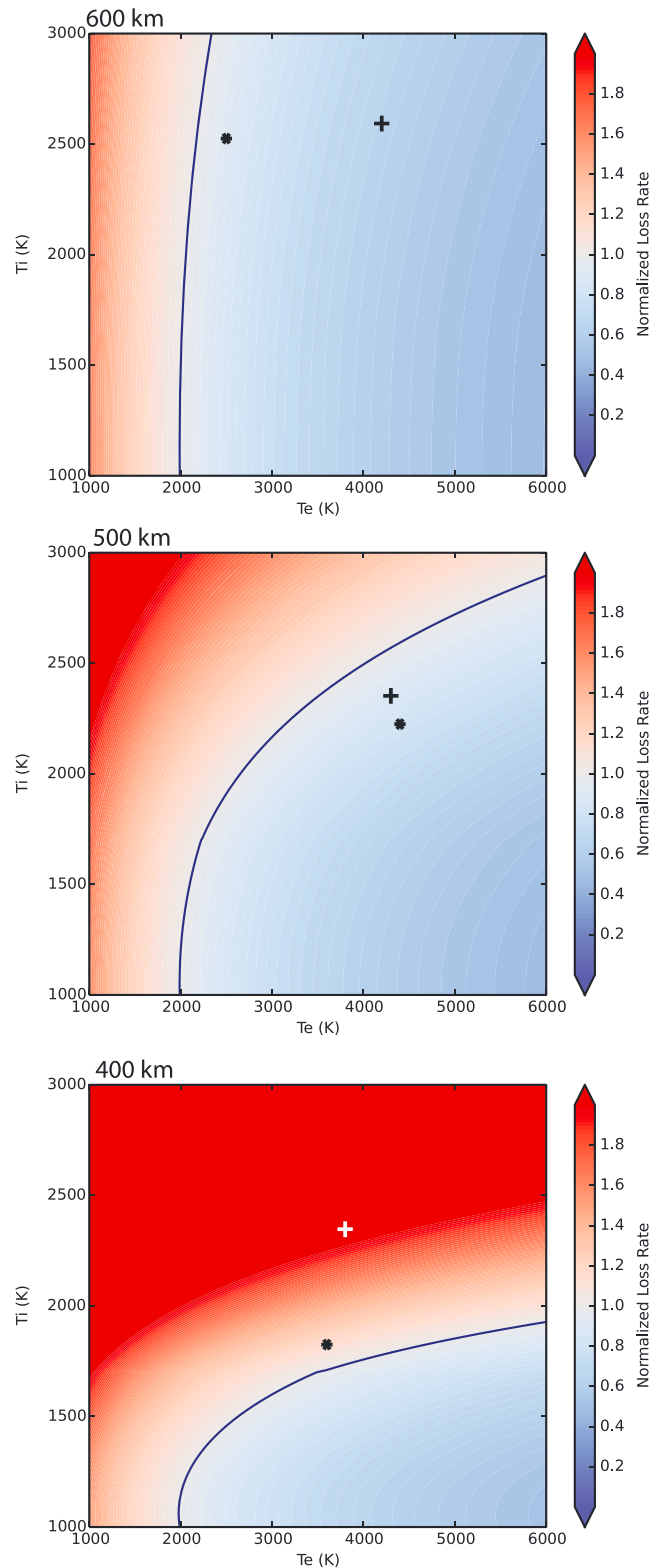
Figure 9. Electron loss rate normalized to quiet time value at 400 km, 500 km, and 600 km are shown. The corresponding T_e and T_i pairs at different altitudes shown in Figure 7 are marked by crosses (beam 2 measurements) and asterisks (beam 4 measurements).

unchanged as previously suggested by *Wahlund et al.* [1992]. Because no simultaneous particle precipitation measurements were included in the *Wahlund et al.* [1992] study, it is difficult to make a direct comparison between our event and theirs. However, we discuss in this section possible mechanisms that could account for the topside ionospheric density increase in this event.

3.2.1. Temperature-Dependent Recombination Rate

During a typical frictional heating (type 1) event, T_i would increase due to the relative motion between ions and neutrals. The increase of T_i accelerates the conversion from atomic ion O^+ to molecular ions NO^+ and O_2^+. The dissociative recombination rates of these two molecular ions are about 5 orders of magnitude larger than the radiative recombination rate of atomic ion O^+. Therefore, the plasma density would decrease rapidly as a result of frictional heating. Previous modeling studies have quantified this effect and suggested it as one of the mechanisms for causing density troughs in the ionosphere [*Sellek et al.*, 1991; *Heelis et al.*, 1993; *Zettergren et al.*, 2015].

However, the dissociative recombination rates of molecular ions are also inversely proportional to T_e. An increase of T_e can reduce the recombination rates and slow down the plasma density decrease. Therefore, the changes of the recombination rate and plasma density depend on the values of both T_i and T_e. Recently, *Zhu et al.* [2016] estimated the electron density loss rate by changing both temperatures and found that high T_e and relatively low T_i tend to reduce the plasma loss rate. Similar calculations of the electron density loss rate relative to quiet time values at 400 km, 500 km, and 600 km are shown in Figures 9a–9c, respectively. Chemical reactions included in the calculation are listed below, including charge exchanges (3–5), dissociative recombinations ((6) and (7)), and radiative recombination (8):
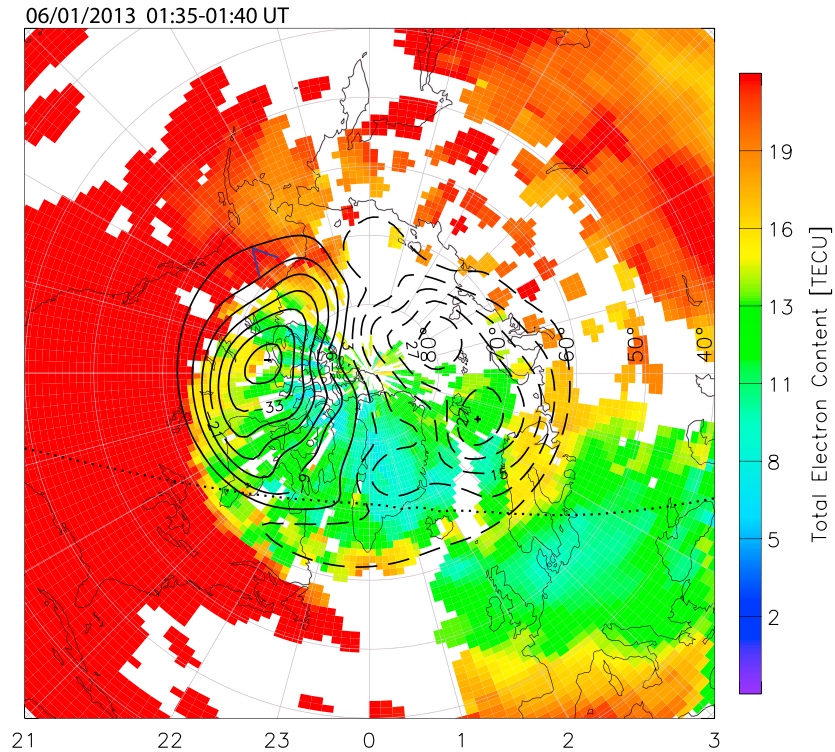
06/01/2013 01:35-01:40 UT

Figure 10. A polar view of the 2-D GPS TEC map at 0140 UT on 1 June 2013 superimposed with the modeled ionospheric $E \times B$ convection pattern based on SuperDARN measurements. The field of view of PFISR is shown by blue segments.

$$O^+ + N_2 \xrightarrow{K1} NO^+ + N \tag{3}$$

$$O^+ + O_2 \xrightarrow{K2} O_2^+ + O \tag{4}$$

$$O^+ + NO \xrightarrow{K3} NO^+ + O \tag{5}$$

$$NO^+ + e^- \xrightarrow{K4} O + N \tag{6}$$

$$O_2^+ + e^- \xrightarrow{K5} O + O \tag{7}$$

$$O^+ + e^- \xrightarrow{K6} O. \tag{8}$$

K1–K6 are plasma temperature-dependent reaction coefficients from Appendix A of *Zhu et al*. [2016]. The background O^+ densities are obtained from the PFISR measurements, and neutral densities are obtained from the aforementioned MSIS model [*Picone et al*., 2002].

The corresponding T_e and T_i pairs at different altitudes shown in Figure 8 are marked in Figure 9 by crosses (beam 2 measurements) and asterisks (beam 4 measurements). The loss rate was normalized to the plasma temperature measured during quiet time, i.e., ~1000 K and ~2000 K for T_i and T_e, respectively. As shown in Figure 8, the electron loss rate during the ion upflow event increased at 400 km and reduced at 500 and 600 km. The electron loss rate below 300 km (not shown) increased significantly.

The calculation shown above suggests that recombination below ~400 km is enhanced, which is responsible for the electron density decrease. However, this effect is weakened in the topside ionosphere due to the significantly increased T_e.

3.2.2. Lifting of Ionosphere Plasma Due To Northward $E \times B$ Drift

Figure 3c shows that after the IMF southward turning at 0130 UT, the enhanced convection flows were in the northwestern direction. Given the ~78° magnetic field inclination angle at PFISR, the projection of these convection flows onto the vertical direction was positive. Figures 3d and 3e show that the averaged vertical flows reached ~100 m/s, and these vertical flows were responsible for the F layer lifting observed by all the

beams. A short period of *F* layer descending after 02 UT was also observed due to a short-lived reduction of convection speed. Lifting the ionosphere to higher altitude away from the dense neutrals would reduce the recombination rate, and consequently, the density in the topside ionosphere would increase. Our observations indicate that the topside ionosphere density at ~600 km increased from $1.48 \times 10^{11}\, \mathrm{m}^{-3}$ before the lifting to $2.24 \times 10^{11}\, \mathrm{m}^{-3}$ after the lifting, i.e., a 54% increase.

Figure 10 shows 2-D GPS TEC map at 0140 UT [*Rideout and Coster*, 2006] superimposed with the modeled ionospheric $E \times B$ convection pattern (solid and dashed black contours) based on Super Dual Auroral Radar Network (SuperDARN) measurements [*Ruohoniemi and Baker*, 1998; *Shepherd and Ruohoniemi*, 2000]. The plot is shown in the MLT and MLAT coordinates with 12 MLT/18 MLT at the top left. The FOV of PFISR in Alaska is marked by the blue segments. The solar terminator is also shown by the dotted line. During the whole course of this event, PFISR, which is located in Alaska, was in the sunlit region. It can be seen that the lifted plasma observed by PFISR is within the SED plume over Alaska.

Recently, *Cohen et al.* [2015] used a one-dimensional numerical simulation to study the effect of topside ionosphere density on ion upflow. They found that while the ambipolar electric field and the upflow speed become smaller as the topside ionosphere density increases, the resulting upflow fluxes actually become larger. Similarly, our analysis presented here suggests that the density increase in the topside ionosphere, due to a combination of lifting by northward $E \times B$ drift and temperature-dependent recombination, plays an important role in producing the intense upward fluxes observed in the 1 June event.

4. Summary and Conclusions

Using observations from multiple instruments and results from a global magnetospheric simulation, we have investigated an intense ion upflow event during the 1 June 2013 geomagnetic storm and provided a more comprehensive mechanism for the generation of intense ion upflows observed in association with SEDs.

The high-latitude convection pattern and the OCB expanded equatorward after the strong IMF southward turning. Divergent ion flows occurred near the OCB, and the intense ion upflow fluxes reached $\sim 1.9 \times 10^{14}\, \mathrm{m}^{-2}\, \mathrm{s}^{-1}$ at ~600 km. Significant increase in both ion and electron temperatures due to particle precipitation associated with dayside magnetopause reconnection has been observed at the same time as the ion divergent flows. In particular, the ion upflow occurred above 450 km, where the ion temperature gradient was positive. Based on this temperature observation and previous simulation results, we suggest that this ion upflow event was mainly caused by the soft electron precipitation and, therefore, should be categorized as a type 2 upflow event. Factors contributing to the high electron density and intense ion upflow fluxes, including plasma temperature effects and preconditioning, have been discussed. We have estimated the electron loss rate using measured plasma temperatures and concluded that because of significantly increased electron temperature, the electron loss rate due to recombination can be reduced at higher altitudes. In addition, this intense ion upflow flux event is preconditioned by lifted *F* region ionosphere due to northwestward convection flows in the SED plume. Results from a global MHD simulation of the magnetosphere using the observed solar wind conditions have been analyzed to understand the unusual MLT locations of the cusp-like particle precipitations observed by the DMSP satellite. Combining the observation and simulation results, we suggest that both soft electron precipitation ($<$100 eV) originating from the dayside magnetopause reconnection, which heats the electrons and reduces the dissociative recombination rate in the topside ionosphere, and the preconditioning of topside ionosphere by SED plasma contribute to the observed electron density increase and intense ion upflow fluxes.

References

Aponte, N., M. J. Nicolls, S. A. Gonzalez, M. P. Sulzer, M. C. Kelley, E. Robles, and C. A. Tepley (2005), Instantaneous electric field measurements and derived neutral winds at Arecibo, *Geophys. Res. Lett.*, *32*, L12107, doi:10.1029/2005GL022609.

Brambles, O. J., W. Lotko, B. Zhang, M. Wiltberger, J. Lyon, and R. J. Strangeway (2011), Magnetosphere sawtooth oscillations induced by ionospheric outflow, *Science*, *332*(2011), 1183–1186, doi:10.1126/science.1202869.

Buchert, S. C., Y. Ogawa, R. Fujii, and A. P. van Eyken (2004), Observations of diverging field-aligned ion flow with the ESR, *Ann. Geophys.*, *22*, 889–899, doi:10.5194/angeo-22-889-2004.

Buonsanto, M. J., and O. G. Witasse (1999), An updated climatology of thermospheric neutral winds and *F* region ion drifts above Millstone Hill, *J. Geophys. Res.*, *104*, 24,675–24,687, doi:10.1029/1999JA900345.

Buzulukova, N., M.-C. Fok, A. Pulkkinen, M. Kuznetsova, T. E. Moore, A. Glocer, P. C. Brandt, G. Tóth, and L. Rastätter (2010), Dynamics of ring current and electric fields in the inner magnetosphere during disturbed periods: CRCM–BATS-R-US coupled model, *J. Geophys. Res.*, *115*, A05210, doi:10.1029/2009JA014621.

Cohen, I. J., M. R. Lessard, R. H. Varney, K. Oksavik, M. Zettergren, and K. A. Lynch (2015), Ion upflow dependence on ionospheric density and solar photoionization, *J. Geophys. Res. Space Physics*, *120*, 10,039–10,052, doi:10.1002/2015JA021523.

Daglis, I. A., R. M. Thorne, W. Baumjohann, and S. Orsini (1999), The terrestrial ring current: Origin, formation, and decay, *Rev. Geophys.*, *37*, 407–438, doi:10.1029/1999RG900009.

De Zeeuw, D. L., S. Sazykin, R. A. Wolf, T. I. Gombosi, A. J. Ridley, and G. Toth (2004), Coupling of a global MHD code and an inner magnetospheric model: Initial results, *J. Geophys. Res.*, *109*, A12219, doi:10.1029/2003JA010366.

Foster, J. C., et al. (2005), Multiradar observations of the polar tongue of ionization, *J. Geophys. Res.*, *110*, A09S31, doi:10.1029/2004JA010928.

Glocer, A., N. Kitamura, G. Toth, and T. Gombosi (2012), Modeling solar zenith angle effects on the polar wind, *J. Geophys. Res.*, *117*, A04318, doi:10.1029/2011JA017136.

Glocer, A., M. Fok, X. Meng, G. Toth, N. Buzulukova, S. Chen, and K. Lin (2013), CRCM + BATS–R–US two–way coupling, *J. Geophys. Res. Space Physics*, *118*, 1635–1650, doi:10.1002/jgra.50221.

Gombosi, T. I., G. Toth, D. L. De Zeeuw, K. C. Hansen, K. Kabin, and K. G. Powell (2002), Semirelativistic magnetohydrodynamics and physics based convergence acceleration, *J. Comput. Phys.*, *177*, 176–205, doi:10.1006/jcph.2002.7009.

Gombosi, T., et al. (2004), Solution-adaptive magnetohydrodynamics for space plasmas: Sun-to-earth simulations, computing in science and engineering, *Front. Simulation*, *6*, 14–35.

Hardy, D. A., L. K. Schmitt, M. S. Gussenhoven, F. J. Marshall, H. C. Yeh, T. L. Schumaker, A. Huber and J. Pantazis (1984), Precipitating electron and ion detectors (SSJ/4) for the block 5D/Flights 6–10 DMSP satellites: Calibration and data presentation, Rep. AFGL-TR-84- 0317, Air Force Geophysics Laboratory, Hanscom AFB, Mass.

Heelis, R. A., G. J. Bailey, R. Sellek, R. J. Moffett, and B. Jenkins (1993), Field-aligned drifts in subauroral ion drift events, *J. Geophys. Res.*, *98*, 21,493–21,499, doi:10.1029/93JA02209.

Heinselman, C. J., and M. J. Nicolls (2008), A Bayesian approach to electric field and *E*-region neutral wind estimation with the Poker Flat Advanced Modular Incoherent Scatter Radar, *Radio Sci.*, *43*, RS5013, doi:10.1029/2007RS003805.

Kronberg, E. A., et al. (2014), Circulation of heavy ions and their dynamical effects in the magnetosphere: Recent observations and models, *Space Sci. Rev.*, *184*, 173–235, doi:10.1007/s11214-014-0104-0.

Liao, J., X. Cai, L. M. Kistler, C. R. Clauer, C. G. Mouikis, B. Klecker, and I. Dandouras (2014), The relationship between sawtooth events and O^+ in the plasma sheet, *J. Geophys. Res. Space Physics*, *119*, 1572–1586, doi:10.1002/2013JA019084.

Liu, C., J. L. Horwitz, and P. G. Richards (1995), Effects of frictional ion heating and soft-electron precipitation on high-latitude *F*-region upflows, *Geophys. Res. Lett.*, *22*, 2713–2716, doi:10.1029/95GL02551.

Lotko, W. (2007), The magnetosphere–ionosphere system from the perspective of plasma circulation: A tutorial, *J. Atmos. Sol. Terr. Phys.*, *69*(2007), 191–211, doi:10.1016/j.jastp.2006.08.011.

Millward, G. H., R. J. Moffett, H. F. Balmforth, and A. S. Rodger (1999), Modeling the ionospheric effects of ion and electron precipitation in the cusp, *J. Geophys. Res.*, *104*, 24,603–24,612, doi:10.1029/1999JA900249.

Moen, J., K. Oksavik, and H. C. Carlson (2004), On the relationship between ion upflow events and cusp auroral transients, *Geophys. Res. Lett.*, *31*, L11808, doi:10.1029/2004GL020129.

Moore, T. E., and G. V. Khazanov (2010), Mechanisms of ionospheric mass escape, *J. Geophys. Res.*, *115*, A00J13, doi:10.1029/2009JA014905.

Moore, T. E., and J. L. Horwitz (2007), Stellar ablation of planetary atmospheres, *Rev. Geophys.*, *45*, RG3002, doi:10.1029/2005RG000194.

Nilsson, H., et al. (2008), Transients in oxygen outflow above the polar cap as observed by the Cluster spacecraft, *Ann. Geophys.*, *26*, 3365–3373, doi:10.5194/angeo-26-3365-2008.

Ogawa, Y., R. Fujii, S. C. Buchert, S. Nozawa, and S. Ohtani (2003), Simultaneous EISCAT Svalbard radar and DMSP observations of ion upflow in the dayside polar ionosphere, *J. Geophys. Res.*, *108*(A3), 1101, doi:10.1029/2002JA009590.

Picone, J. M., A. E. Hedin, D. P. Drob, and A. C. Aikin (2002), NRLMSISE-00 empirical model of the atmosphere: Statistical comparisons and scientific issues, *J. Geophys. Res.*, *107*(A12), 1468, doi:10.1029/2002JA009430.

Powell, K. G., P. L. Roe, T. J. Linde, T. I. Gombosi, and D. L. de Zeeuw (1999), A solution-adaptive upwind scheme for ideal magnetohydrodynamics, *J. Comput. Phys.*, *154*, 284–309, doi:10.1006/jcph.1999.6299.

Pryse, S. E., A. M. Smith, I. K. Walker, and L. Kersley (2000), Multi-instrument study of footprints of magnetopause reconnection in the summer ionosphere, *Ann. Geophys.*, *18*, 1118–1127, doi:10.1007/s00585-000-1118-3.

Reiff, P. H., T. W. Hill, and J. L. Burch (1977), Solar wind plasma injection at the dayside magnetospheric cusp, *J. Geophys. Res.*, *82*, 479–491, doi:10.1029/JA082i004p00479.

Richards, P. G. (1995), Effects of auroral electron precipitation on topside ion outflows, in *Cross-Scale Coupling in Space Plasmas*, edited by J. L. Horwitz, N. Singh and J. L. Burch, AGU, Washington, D. C., doi:10.1029/GM093p0121.

Rideout, W., and A. Coster (2006), Automated GPS processing for global total electron content data, *GPS Solutions*, *10*(3), 219–228, doi:10.1007/s10291-006-0029-5.

Ridley, A. J., and M. W. Liemohn (2002), A model-derived description of the penetration electric field, *J. Geophys. Res.*, *107*(A8), 1151, doi:10.1029/2001JA000051.

Ridley, A. J., T. I. Gombosi, and D. L. De Zeeuw (2004), Ionospheric control of the magnetosphere: Conductance, *Ann. Geophys.*, *22*, 567, doi:10.5194/angeo-22-567-2004.

Ruohoniemi, J. M., and K. B. Baker (1998), Large-scale imaging of high-latitude convection with Super Dual Auroral Radar Network HF radar observations, *J. Geophys. Res.*, *103*, 20,797–20,811, doi:10.1029/98JA01288.

Sánchez, E. R., and A. StrØmme (2014), Incoherent scatter radar-FAST satellite common volume observations of upflow-to-outflow conversion, *J. Geophys. Res. Space Physics*, *119*, 2649–2674, doi:10.1002/2013JA019096.

Schunk, R., and A. Nagy (2009), *Ionospheres: Physics, Plasma Physics, and Chemistry*, Cambridge Univ. Press, Cambridge.

Sellek, R., G. J. Bailey, R. J. Moffett, R. A. Heelis, and P. C. Anderson (1991), Effects of large zonal plasma drifts on the subauroral ionosphere, *J. Atmos. Terr. Phys.*, *53*, 557–565, doi:10.1016/0021-9169(91)90083-J.

Semeter, J., C. J. Heinselman, J. P. Thayer, R. A. Doe, and H. U. Frey (2003), Ion upflow enhanced by drifting *F*-region plasma structure along the nightside polar cap boundary, *Geophys. Res. Lett.*, *30*(22), 2139, doi:10.1029/2003GL017747.

Seo, Y., J. L. Horwitz, and R. Caton (1997), Statistical relationships between high-latitude ionospheric *F* region/topside upflows and their drivers: DE 2 observations, *J. Geophys. Res.*, *102*, 7493–7500, doi:10.1029/97JA00151.

Shepherd, S. G., and J. M. Ruohoniemi (2000), Electrostatic potential patterns in the high-latitude ionosphere constrained by SuperDARN measurements, *J. Geophys. Res.*, *105*, 23,005–23,014, doi:10.1029/2000JA000171.

Skjæveland, Å., J. Moen, and H. C. Carlson (2014), Which cusp upflow events can possibly turn into outflows?, *J. Geophys. Res. Space Physics*, *119*, 6876–6890, doi:10.1002/2013JA019495.

Strangeway, R. J., R. E. Ergun, Y.-J. Su, C. W. Carlson, and R. C. Elphic (2005), Factors controlling ionospheric outflows as observed at intermediate altitudes, *J. Geophys. Res.*, *110*, A03221, doi:10.1029/2004JA010829.

Su, Y.-J., R. G. Caton, J. L. Horwitz, and P. G. Richards (1999), Systematic modeling of soft-electron precipitation effects on high-latitude *F* region and topside ionospheric upflows, *J. Geophys. Res.*, *104*, 153–163, doi:10.1029/1998JA900068.

Tóth, G., et al. (2012), Adaptive numerical algorithms in space weather modeling, *J. Computational Phys.*, *231*, 870–903, doi:10.1016/j.jcp.2011.02.006.

Tu, J.-N., M. Dhar, P. Song, B. W. Reinisch, J. L. Green, R. F. Benson, and A. J. Coster (2007), Extreme polar cap density enhancements along magnetic field lines during an intense geomagnetic storm, *J. Geophys. Res.*, *112*, A05201, doi:10.1029/2006JA012034.

Wahlund, J.-E., H. J. Opgenoorth, I. Häggström, K. J. Winser, and G. O. L. Jones (1992), EISCAT observations of topside ionospheric ion outflows during auroral activity: Revisited, *J. Geophys. Res.*, *97*, 3019–3037, doi:10.1029/91JA02438.

Yau, A. W., and M. André (1997), Sources of ion outflow in the high latitude ionosphere, *Space Sci. Rev.*, *80*, 1–25, doi:10.1023/A:1004947203046.

Yau, A. W., W. K. Peterson, and T. Abe (2011), Influences of the ionosphere, thermosphere and magnetosphere on ion outflows, in *The Dynamic Magnetosphere, IAGA Special Sopron Book Series*, vol. 3, edited by A. W. Yau, W. K. Peterson, and T. Abe, pp. 283–314, Springer, Netherlands, doi:10.1007/978-94-007-0501-2_16.

Yu, Y., and A. J. Ridley (2013), Exploring the influence of ionospheric O^+ outflow on magnetospheric dynamics: Dependence on the source location, *J. Geophys. Res. Space Physics*, *118*, 1711–1722, doi:10.1029/2012JA018411.

Yuan, Z.-G., X.-H. Deng, and J.-F. Wang (2008), DMSP/GPS observations of intense ion upflow in the midnight polar ionosphere associated with the SED plume during a super geomagnetic storm, *Geophys. Res. Lett.*, *35*, L19110, doi:10.1029/2008GL035462.

Zeng, W., and J. L. Horwitz (2007), Formula representation of auroral ionospheric O^+ outflows based on systematic simulations with effects of soft electron precipitation and transverse ion heating, *Geophys. Res. Lett.*, *34*, L06103, doi:10.1029/2006GL028632.

Zeng, W., and J. L. Horwitz (2008), Storm enhanced densities (SED) as possible sources for Cleft Ion Fountain dayside ionospheric outflows, *Geophys. Res. Lett.*, *35*, L04103, doi:10.1029/2007GL032511.

Zettergren, M. D., J. L. Semeter, and H. Dahlgren (2015), Dynamics of density cavities generated by frictional heating: Formation, distortion, and instability, *Geophys. Res. Lett.*, *42*, 10,120–10,125, doi:10.1002/2015GL066806.

Zhu, J., A. J. Ridley, and Y. Deng (2016), Simulating electron and ion temperature in a global ionosphere thermosphere model:Validation and modeling an idealized substorm, *J. Atmos. Sol. Terr. Phys.*, *138–139*, 243–260, doi:10.1016/j.jastp.2016.01.005.

Zou, S., A. J. Ridley, M. B. Moldwin, M. J. Nicolls, A. J. Coster, E. G. Thomas, and J. M. Ruohoniemi (2013), Multi-instrument observations of SED during 24–25 October 2011 storm: Implications for SED formation processes, *J. Geophys. Res. Space Physics*, *118*, 7798–7809, doi:10.1002/2013JA018860.

Zou, S., M. B. Moldwin, A. J. Ridley, M. J. Nicolls, A. J. Coster, E. G. Thomas, and J. M. Ruohoniemi (2014), On the generation/decay of the storm-enhanced density plumes: Role of the convection flow and field-aligned ion flow, *J. Geophys. Res. Space Physics*, *119*, 8543–8559, doi:10.1002/2014JA020408.